

William R. Palfey^{1,*}, George R. Rossman¹, William A Goddard III²

¹ Division of Geological and Planetary Sciences, California Institute of Technology, Pasadena, CA, 91125, USA

² Materials and Process Simulation Center (MSC), MC 139-74, California Institute of Technology, Pasadena CA, 91125, USA

* To whom correspondence is to be addressed: wpalfey@caltech.edu

ORCID: WAG 0000-0003-0097-5716; WRP 0000-0002-9555-7877; GRR 0000-0002-4571-6884

Key Points:

- DFT calculations predict that quenched hydrous stishovite with a hydrogarnet-type defect exhibits a **tetrahedral configuration**
- At elevated temperatures, we predict that a **square planar defect** configuration also becomes important
- The hydrogarnet defect explains the vibrational spectroscopy of stishovite, with the possible exception of some modes near 1420 cm^{-1}

Abstract

Dense polymorphs of silica have been demonstrated experimentally to incorporate from 1.5% to as much as 11.6% weight percent H_2O as OH groups, with implications for the hydrogen budgets of Earth and other planets. This OH is thought to enter the SiO_2 structure via a charge-balanced substitution in which silicon vacancies (V_{Si}) are compensated by protonating four of the surrounding six oxygen atoms, often referred to as a hydrogarnet-type defect. There are many possible configurations for this defect structure in dense silica, but the nature of these configurations and whether they can be distinguished experimentally is unknown. We present here density functional theory (DFT) calculations that systematically assess the possible configurations of a hydrogarnet-type defect in stishovite (rutile-type SiO_2), with direct comparisons to experimental vibrational spectroscopy data. We predict that stishovite synthesized at 450 K and 10 GPa quenched to room temperature is dominated by a single defect type with tetrahedral geometry. This leads to OH stretching modes ($2500\text{-}3000\text{ cm}^{-1}$) and SiOH bending modes ($\sim 1400\text{ to }1450\text{ cm}^{-1}$) largely consistent with experimentally observed modes. One remaining issue is that our calculations produce results compatible with experimental data on H to D exchange, but do not explain why a considerable fraction of the 1420 cm^{-1} mode shifts by only 40 cm^{-1} in deuterated samples. At elevated pressures and temperatures, we find that a second square planar defect configuration also becomes favorable, leading to modes that should allow differentiation from the tetrahedral configuration.

Plain Language Summary

High pressure experiments mimicking the conditions of Earth's interior have shown that silica minerals present in the mantle can contain large concentra-

tions of hydrogen impurities. These impurities can be detected through infrared spectroscopy, but the positions of hydrogen atoms in the silica structure are unknown. We have used quantum mechanics calculations to predict both the arrangements of hydrogen atoms in high pressure silica and the expected infrared signals corresponding to those arrangements. Although previous authors thought that a variety of hydrogen arrangements are likely in silica, we find that only one arrangement is likely to be important. We have shown that this single arrangement produces an infrared spectrum similar to experimental data. High pressure silica is thought to be an important reservoir for hydrogen in the earth, making our results key for understanding how hydrogen is sequestered in these minerals.

1 Introduction

Stishovite has long been established as an important phase among nominally anhydrous minerals (NAMs). Previous experimental work revealed that stishovite is capable of incorporating H_2O in concentrations up to 0.3 weight percent via a coupled substitution involving Al^{3+} (Litasov et al., 2007; Pawley et al., 1993), in a manner similar to coupled substitutions in rutile (Bromiley & Hilairet, 2005; Koudriachova et al., 2004). This resembles the mantle-stable phases $-\text{AlOOH}$ and phase H ($\text{MgSiO}_2(\text{OH}_2)$), among others. Such coupled substitutions were previously accepted as the primary manner by which hydrogen is dissolved in stishovite in the high temperature and pressure conditions of the lower mantle.

However, subsequent work by Spektor et al. (2011) showed that stishovite is also capable of incorporating up to 3 wt% H_2O in the absence of Al at temperature and pressure conditions of 400 to 550 °C and 10 GPa^{5,6}, a result confirmed by both Spektor et al. (2016) and Nisr et al. (2017). Further synthesis experiments by Lin et al. (2020) and Nisr et al. (2020) found that hydrous Al-free dense silica phases (including CaCl_2 - and niccolite-type SiO_2) remain stable at significantly higher pressures (up to 55 GPa) and temperatures (up to 1835 K) incorporating even higher concentrations of H_2O upon successive phase transitions (possibly up to 11.3 wt%). These experiments suggest that dense silica phases may provide a hydrogen reservoir beyond subduction zones into deeper mantle regimes and large planetary interiors.

Hydrogen is thought to be incorporated into Al-free stishovite at a Si vacancy on a tetrahedral site ($(\text{SiO}_4)^{4-}$), which is charge compensated by forming four OH groups ($(\text{OH}^-)_4$) around the vacancy (Spektor et al., 2011). This is similar to the hydrogarnet defect in Ca-rich garnets. In the six-coordinate stishovite system, such a defect is also structurally analogous to Ruetschi defects found in various MnO_2 polymorphs, where protons compensate for Mn (IV) vacancies (Ruetschi, 1984). Similar structures have also been proposed as possible defects in rutile-type TiO_2 (Bjørheim et al., 2013). Nuclear magnetic resonance (NMR) studies carried out by Spektor et al. (2011) and Spektor et al. (2016) revealed that certain populations of H in Al-free hydrous stishovite correlate directly to Si, implying a possible link to Si vacancies, congruent with a hydrogarnet-type defect.

Spektor et al. (2011, 2016) also concluded from their NMR studies that multiple configurations of these Si-linked hydrogens are likely to coexist in stishovite. However, they did not propose a particular set of configurations. Subsequent Raman measurements by Nisir et al. (2017) observed several OH modes suggesting coexistence of multiple types of hydrogarnet defects. However, it is unclear if the multiple modes are due to multiple defect configurations, lower symmetry defects, or proton dynamics. Additionally, infrared data from Spektor et al. (2011, 2016) show the existence of sharp bands centered at 1420 cm^{-1} associated with hydrogen, possibly related to SiOH bending.

Here, we use density functional theory (DFT) methods to predict the energies, geometries, and OH vibrational frequencies for configurations of OH surrounding the V_{Si} site in stishovite. We predict the most energetically favorable configurations of the $(\text{OH}^-)_4$ Ruetschi-like hydrogarnet defect in stishovite, the positions of their associated hydrogen-related vibrational modes, and their behavior at the synthesis and analysis conditions of Spektor et al. (2011 and 2016).

2 Materials and Methods

2.1 Details of Calculations

We performed three varieties of calculations: structural minimizations, phonon calculations of the minimized structures using density functional perturbation theory (DFPT), and quantum mechanics molecular dynamics (QM MD) at various temperatures and pressures. All DFT calculations used the Vienna Ab initio Simulation Package (VASP, version 5.4.4.18Apr17). These calculations used the Perdew-Burke-Ernerhof (PBE) generalized gradient approximation to describe the exchange correlation (Blöchl, 1994; Kresse & Furthmüller, 1996a, 1996b; Kresse & Hafner, 1993; Kresse & Joubert, 1999; Perdew et al., 1996; Perdew et al., 1997), along with the empirical D3 van Der Waals correction (Grimme et al., 2010, 2011). The cutoff energy for the plane-wave basis set was 500 eV and energy smearing near the Fermi energy was handled through the tetrahedron method with a smearing width of 0.05 eV and Blöchl corrections (Blöchl et al., 1994). A $5\times 5\times 5$ Monkhorst–Pack mesh was found to be sufficient to optimize structures for our unit cell size (discussed below) to converge energy values within 1 meV for structural minimizations. Atomic forces were minimized to a value of $0.01\text{ eV}/\text{Å}$. The DFPT calculations used a reduced $2\times 2\times 2$ K-point mesh and estimated infrared intensities were calculated from the Born effective charges.

QM MD was performed via VASP using an NVT ensemble, with 1 fs time steps and temperature corrections every 40 fs. These parameters were found to be sufficient for stabilizing temperature, pressure, and the kinetic and potential energies of the simulated system. For all configurations tested, the QM MD calculations consisted of three parts: heating the system from 10 K to the target temperature over the course of 10 ps, allowing the system to equilibrate at the target temperature for 3 ps, and holding the system at the target temperature for 20 ps. The final 20 ps run was then used to calculate the temperature,

pressure, and energy of the system at simulated conditions.

QM MD calculations were carried out at four different temperatures: 450 °C (representing optimal experimental synthesis conditions from Spektor et al. (2016)), 25 °C (representative of the conditions under which experimental data were collected on quenched samples), 500 °C (to estimate behavior just above optimal conditions) and 262 °C (the temperature halfway between the highest and lowest simulated). The results of the QM-MD calculations were then used for two phase thermodynamics (2PT) analyses (Lin et al., 2003; Lin et al., 2010; Pascal et al., 2011) to generate the phonon density of states and thermodynamic properties for each case.

2.2 Creation of Defect Structures

We used a $2 \times 2 \times 3$ unit cell containing 24 Si sites and 48 O sites. When one Si atom is removed and four H are placed in the $2 \times 2 \times 3$ cell, the resulting concentration of H_2O is 2.54 wt%. For all calculations, the unit cell parameters were fixed at $a=4.1953 \text{ \AA}$, $c=2.665 \text{ \AA}$, consistent with the dimensions measured for hydrous, Al-free stishovite by Spektor et al. (2011) and Spektor et al. (2016). This corresponds to ~ 2.0 wt% H_2O at 10 GPa (Nisr et al., 2017).

A conventional hydrogarnet defect occurs on a tetrahedral Si site, where all four O atoms surrounding V_{Si} form OH bonds. In contrast, the Ruetschi-style hydrogarnet defect proposed for stishovite occurs on a distorted octahedral Si site, leading to many possible configurations for the four OH. This has been suggested by prior authors as a factor contributing to the breadth of the OH bands observed in Al-free stishovite (Spektor et al., 2011). Additionally, other systems with six-coordinate silica have been predicted to simultaneously incorporate several configurations of hydrogarnet-type defects (Shim et al., 2022). Thus, to thoroughly test the likely arrangement of OH around V_{Si} , we tested many arrays of OH, taking into account both the selection of O sites for protonation and the resulting OH orientations.

Our initial studies of various configurations revealed that OH almost exclusively orients itself skew to both a and c , at a slight slant from the edges of the octahedral Si site, regardless of starting position. Subsequent configurations tested were restricted to include only OH oriented in this manner. Operating under this constraint, and accounting for the orthorhombic symmetry of the V_{Si} site, we derived and tested 26 possible arrangements for 4 OH groups around V_{Si} (Details of these arrangements are found in the supplementary material).

3 Results

3.1 Structural minimizations

Starting with the 26 possible unique arrays of OH around V_{Si} , we found that all configurations converged to just one of seven structures, briefly summarized below:

- The most favorable configuration is the tetrahedral case shown in Figure 1. This is the only structure important at 25 °C
- The next most favorable is the square planar case shown in Figure 1. It is ~0.140 eV higher energy than the tetrahedral case. Based on this energy difference, it would be populated ~0.65% at 25 °C and ~11.5% at 450 °C.
- The other five cases have energies ~0.50 to 1.31 eV higher and hence are not important at temperatures of 450 °C and below.

Thus, we predict that **only two configurations are likely to be relevant in Al-free stishovite** at elevated temperatures and only one is important at 298 K. We focused on just these two structures for the remaining calculations. Models of the two structures are presented in Figure 1. Details of the remaining five configurations are in the supplementary material.

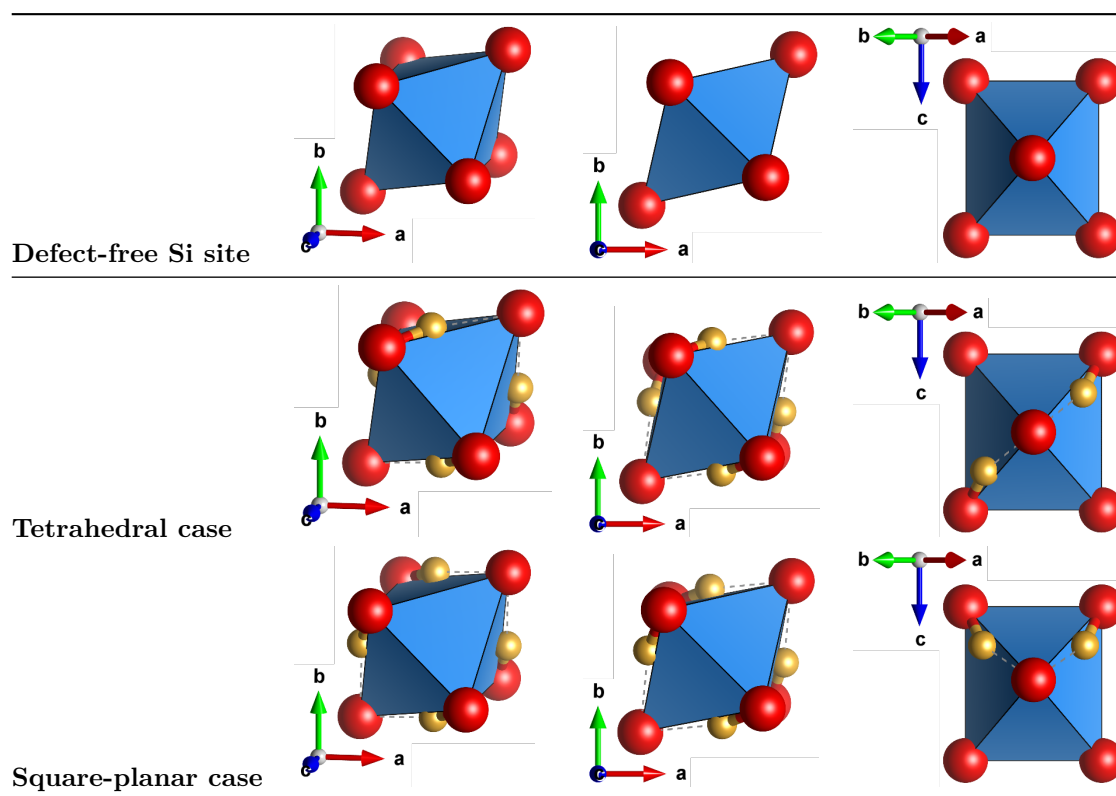


Figure 1. Different views of the ideal Si site in stishovite (top row), the tetrahedral case (middle row) and the square planar case (bottom row). In the tetrahedral case, OH on opposing corners hydrogen bond to the same axial atom, while in the square planar case, OH that are c-parallel hydrogen bond to

the same axial atom.

3.1.1 The tetrahedral case

The lowest energy configuration consists of OH groups populating only the four basal O atoms of the octahedral Si site. All OH bonds are oriented such that they are slightly skew to the edges of the V_{Si} octahedron, forming hydrogen bonds with one of the two axial O atoms having no H. The OH orientations alternate, with OH on opposing corners of the octahedral base pointing to the same axial O atom. This results in the H atoms forming a tetrahedral shape around V_{Si} , as has been suggested by Spektor et al. (2011). All four $d(O-H \cdots O)$ are ~ 2.55 Å, while H atoms hydrogen bonded to the same axial O atoms are separated by 2.22 Å. The slight skew of the OH groups off of the octahedral edges gives the defect site an overall C_2 symmetry.

3.1.2 The square planar case

The second lowest energy configuration also consists of four OH groups on the basal O atoms surrounding V_{Si} , with hydrogen bonding to axial O atoms. However, in contrast to the tetrahedral case, the OH groups form c -perpendicular pairs, each pointing to the same axial O atom. This results in the H atoms forming a square planar configuration. All four $d(O-H \cdots O)$ are ~ 2.52 Å, while H atoms hydrogen bonded to the same axial O atoms are separated by only 1.82 Å, significantly closer than in the tetrahedral case and likely responsible for the higher energy. An alternate square planar configuration with c -parallel OH pairs, rather than c -perpendicular pairs, leads to an energy 0.67 eV higher. This is likely due to decreased H-H distances (1.57 Å) resulting in increased H-H repulsion. The square planar defect site has C_{2h} symmetry. It is 0.14 eV higher energy than the tetrahedral case.

3.2 Vibrational modes calculated using DFPT

DFPT calculations predict that both the tetrahedral and square planar cases should produce multiple infrared-active OH stretching and bending modes. The predicted stretching modes are positioned from 2704 to 2871 cm^{-1} for the tetrahedral case and 2683 to 2887 cm^{-1} for square planar, all within range of the modes observed by Spektor et al. (2011, 2016). The two SiOH bending modes for the tetrahedral case are at 1420 and 1362 cm^{-1} while they are at 1520 and 1390 cm^{-1} for the square planar case. Given the predicted abundances of the tetrahedral and square planar defects, the tetrahedral case explains the 1420 cm^{-1} mode observed experimentally (see Figure 2 and Table 1). The SiOH bending modes are calculated to have a significantly lower infrared activity compared to the OH stretching modes.

These trends hold true for the calculated deuterium modes. Here the SiOH bending mode for the tetrahedral case that explains the experimental ~ 1420 cm^{-1} mode should move to 1069 cm^{-1} upon deuteration. Although part of the 1420 cm^{-1} mode is observed experimentally to shift to 1079 cm^{-1} , most of it shifts only to 1383 cm^{-1} .

Three OH stretching modes are predicted to be infrared active for the tetrahedral defect:

- 2871 cm^{-1} corresponds to symmetric stretching of OH on opposing corners, maintaining the overall C_2 symmetry of the site.
- 2750 cm^{-1} corresponds to the symmetric combination of OH stretches of the c -perpendicular pairs
- 2704 cm^{-1} corresponds to the symmetric combination of OH stretches of c -parallel pairs.

The latter two modes break the C_2 symmetry of the site while maintaining all H-H distances. The square planar defect is predicted to have two infrared-active modes:

- 2887 cm^{-1} corresponds to symmetric stretching of the c -perpendicular OH pairs
- 2683 cm^{-1} corresponds to symmetric stretching of the c -parallel pairs.

For both the tetrahedral and square planar defects, OH bonds are oriented skew to both c and a such that OH stretching modes should be of roughly equivalent intensity regardless of polarization direction. The same holds true for the bending modes of the tetrahedral case, but not the square planar case, where bending modes are polarized strongly perpendicular to the c -axis.

Tetrahedral:			Square Planar:		
Motion	OH (cm^{-1})	OD (cm^{-1})	Motion	OH (cm^{-1})	OD (cm^{-1})
OX stretch	2871	2099	OX stretch	2887	2109
	2750	2012		2683	1968
	2704	1983		Si-OX bend	1520
Si-OX bend	1420	1069		1390	1055
	1362	1030			

Table 1. Summary of the infrared active OH and OD stretching and bending modes for the tetrahedral case (left) and the square planar case (right). Note that additional OH/OD modes are, strictly speaking, infrared-active, but their predicted intensities are several orders of magnitude lower and unlikely to be observed experimentally.

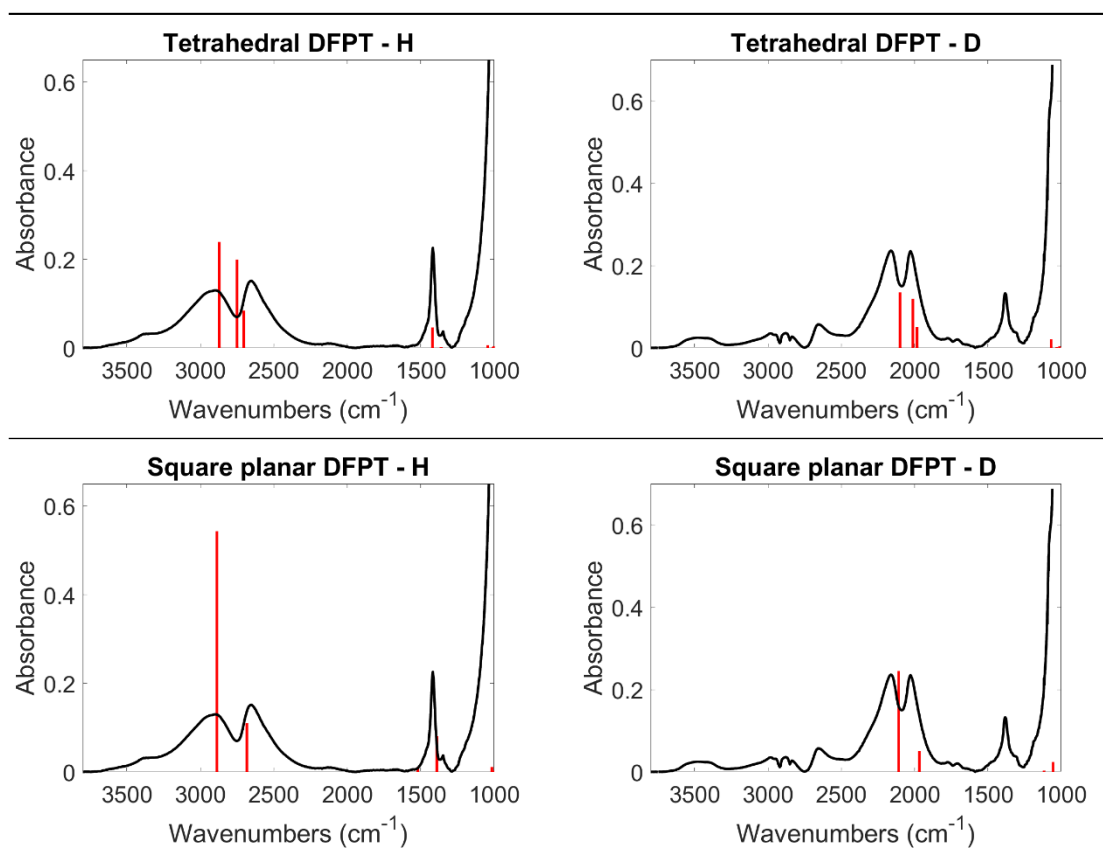


Figure 2. Comparisons between the experimental data of Spektor et al., 2016 (black) and DFPT calculated modes, weighted by calculated intensities (red vertical lines). DFPT modes in the upper two plots were calculated from the tetrahedral case, while the lower two plots were calculated from the square planar case. Both hydrogen (left) and deuterium (right) are presented.

3.3 QM molecular dynamics and 2PT analysis

For static (0 K) calculations, the tetrahedral case is energetically preferable to the square planar case by 0.140 eV. For our molecular dynamics calculations we calculate the Boltzmann factor at each temperature. We find that the proportion of tetrahedral to square planar defects should be 111:1 at 25 °C but it becomes 50:46 at 500 °C (see Table 2). Because we performed NVT dynamics, the external pressure is not constrained, resulting in different pressure values for each temperature. We include the resulting total pressure values (combined external and kinetic pressure terms) in Table 2, along with the total energy (summed potential and kinetic energies) and temperature, which varies slightly between simulations.

Tetrahedral case:		Square planar case:			
Run	Energy (eV)	Pressure (kB)	Temperature (K)	Energy (eV)	Pr
0 K	-571.192	76.3	N/A	-571.052	77.
25 ° C	-564.061	93.7	296.5	-563.942	97.
262 ° C	-559.532	108.4	532.4	-559.426	113
450 ° C	-555.895	118.3	719.2	-555.827	125
500 ° C	-554.879	121.9	768.8	-554.873	127

Table 2. Average total energy, pressure, and temperature values for each QM MD simulation. The Boltzmann factor for the square planar case at each simulated condition (based on average temperatures between the simulations) is also presented. The 0 K values from the minimized structure are also presented in the top row.

The phonon densities of states from the 2PT analysis for each dynamics run are presented in Figure 3. For the tetrahedral case, predicted modes in the SiOH bending region consist of three distinct peaks at 25 ° C, but with increasing temperatures and pressures, they broaden and become less distinct. These SiOH bending modes are predicted at the same position as the mysterious 1420 cm^{-1} peak observed by Spektor et al. (2011, 2016).

The square planar phonon densities predict OH stretches to have a close distribution of modes at room temperature, broadening less than the OH modes of the tetrahedral case with increased pressure and temperature, while also producing modes at significantly lower and higher frequencies. This might be due to increased hydrogen bonding with oxygen (lower $d(\text{O-H} \cdots \text{O})$) and increased H-H repulsion, as proposed by Nisr et al. (2017). Notably, the square planar structure results in no features in the $\sim 1420 \text{ cm}^{-1}$ region, in contrast with experimental data.

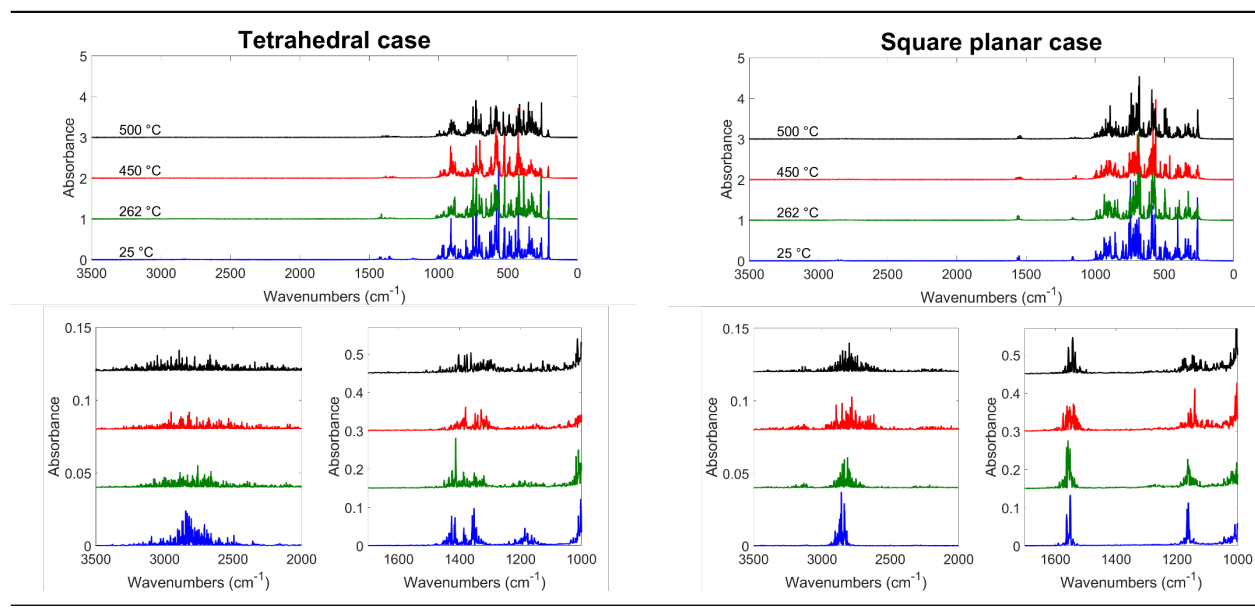


Figure 3. The phonon density of states for the tetrahedral case (left) and square planar case (right) at each simulated temperature (25 °C, 262 °C, 450 °C and 500 °C). Enlarged plots of the OH stretching and bending regions are presented for each case. For both defect configurations, increasing the pressure and temperature significantly broadens the OH stretching and SiOH bending modes. Notably, the tetrahedral case produces a wide distribution of OH stretches even at 25 °C. Thus, the single tetrahedral case can explain the multiple bands observed experimentally. Most important is that the tetrahedral case finds the SiOH bending modes at $\sim 1420 \text{ cm}^{-1}$ whereas the square planar case puts this above 1500 cm^{-1} .

4 Discussion

Our structural minimization and QM MD calculations at 298K predict that the important configuration for the hydrogarnet-type defect in stishovite at 25 °C is the tetrahedral case. This tetrahedral model is similar to the one proposed by Spektor et al., 2011. However, **our calculations predict that only the tetrahedral defect configuration is important** at 25 °C. The tetrahedral defect structure explains the several OH modes observed experimentally, in contrast to the multiple defect states suggested to explain the broad distribution of vibrational modes proposed previously. We find the square planar configuration has a population of 1% at 25 °C, but a population of 45% at 450 °C. Thus, the square planar configuration is relevant only at the pressure and temperatures of synthesis (450 °C and 10 GPa) and higher.

Overall, our QM calculated OH modes match the infrared data of Spektor et al. (2011, 2016), with only a few minor incongruences. The broad OH modes cen-

tered at 2904 and 2656 cm^{-1} present in low-temperature-synthesized stishovite can be compared to predicted modes at 2704, 2750, and 2871 cm^{-1} for the tetrahedral defect and 2683 and 2887 cm^{-1} for the square planar defect. These two defect structures are consistent with the experimental data, since the short hydrogen bonding distances in these defects correspond to low cm^{-1} OH modes, as detailed in Libowitzky et al. (1999).

Calculated stretching modes for deuterium similarly match the experimental OD modes. Our tetrahedral hydrogarnet-type defect also explains the “mysterious” modes observed by Spektor et al. (2011, 2016) centered near 1420 cm^{-1} . Our results indicate that the tetrahedral planar defects produce SiOH bending modes near 1420 cm^{-1} , whereas square planar defect leads to modes at 1390 cm^{-1} and above 1500 cm^{-1} . Upon deuteration, our calculations predict that the bending mode shifts to 1069 cm^{-1} , within 10 cm^{-1} of a mode observed in the infrared data of Spektor et al. (2016). However, it is important to note that although some deuterium modes shift by the magnitude expected for the SiOH bend, a significant population shifts by only about 40 cm^{-1} down to 1383 cm^{-1} . This suggests that, although the 1420 cm^{-1} mode is associated with hydrogen, some of the modes in the 1420 cm^{-1} region may not be due to SiOH bending.

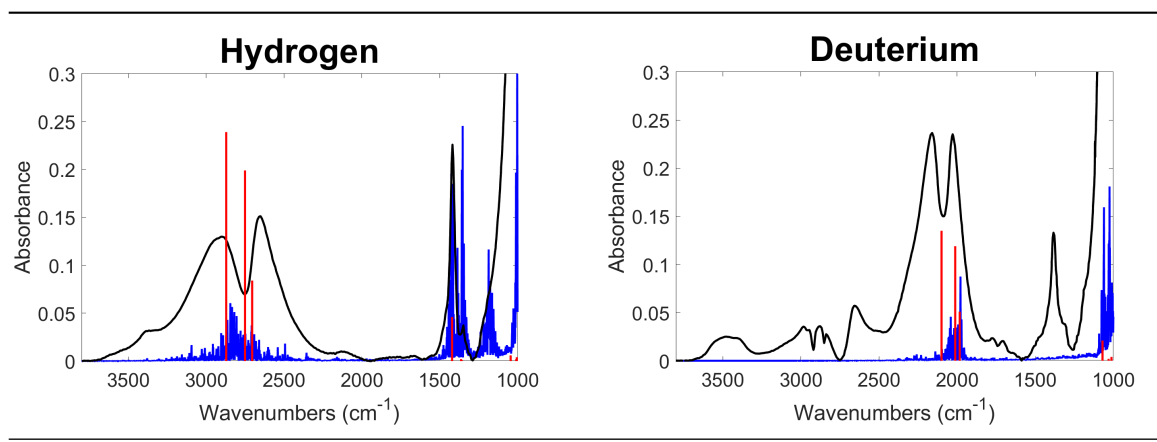


Figure 4. Comparison of the predicted QM modes at 0K (red) and the vibrational density of states (DoS) at 298 K (blue) from 2PT for the tetrahedral defect with the experimental spectrum (black) from Spektor et al. (2016). Spectra for both hydrogen (left) and deuterium (right) are presented. In addition to general consistency between the predicted DoS spectrum and experiment for OH stretches and SiOH bends, the 2PT calculations accurately predict modes present near 1200 cm^{-1} found in the experiment. OD stretches generally match the experimental data, but there is notably no vibrational mode predicted near the 1383 cm^{-1} mode, suggesting it is not due to SiOD bending.

Our predicted vibrational DoS provides additional insight into the behavior of

the hydrogarnet-type defect in stishovite. The 298 K spectra of the tetrahedral case shows behavior largely consistent with the infrared data presented by Spektor et al. (2011, 2016); the OH modes are broad and located in the range of $2500 - 3000 \text{ cm}^{-1}$, with a possible separation between two groups of modes. In contrast, the square planar case forms a narrower cluster of OH modes at higher energy. Most importantly, the $\sim 1420 \text{ cm}^{-1}$ bending mode is present in the tetrahedral case spectra, but this feature is at $\sim 1550 \text{ cm}^{-1}$ in the square planar spectrum. **This indicates that the tetrahedral structure is truly dominant in quenched hydrous stishovite.** Although we predict the square planar case exists in negligible quantities in quenched samples, this defect square should have comparable abundances to the tetrahedral defect at the synthesis temperature of $450 \text{ }^\circ\text{C}$ and 10 GPa . Thus, we expect these higher wavenumber OH bending modes to emerge when measurements are taken in situ.

Previous authors have attributed the broadness of the OH bending modes in hydrous stishovite to the coexistence of multiple tetrahedral configurations. Instead, our calculations show that the breadth of predicted OH modes for just the single tetrahedral case is comparable to the experimental data (Figure 4). The inclusion of proton dynamics, resulting in a high variability of $d(\text{O-H} \cdots \text{O})$, and H-H repulsion induced by molecular dynamics simulations produces significant peak broadening, even at room temperature. Thus, we find that **our single tetrahedral defect is sufficient to explain the observed OH character in hydrous stishovite at room temperature.**

Nonetheless, it is possible that additional defect configurations may be present. For example, clusters of hydrogarnet-type defects could exist between adjacent V_{Si} sites, such as has been suggested by Nisir et al. (2017), leading to a wider range of hydrogen bonding distances and lower local symmetries. Such clusters almost certainly exist in extremely hydrous ($\sim 4.3\% +$), high pressure dense silica, as was synthesized by Nisir et al. (2020). At these concentrations, the $(\text{OH})_4$ defect density would be such that directly adjacent defects would be inevitable.

Other native defects could also couple to hydrogen in stishovite. These types of defects are well-documented in the rutile system and could result in OH modes more consistent with some experimental data. Specifically, Litasov et al. (2007) and others report OH modes from 3312 to 3189 cm^{-1} polarized perpendicular to the c -axis in systems for which Al concentrations are too low to account for all hydrogen incorporated. In such defects, OH would orient in a manner similar to the “channel centered” orientation described for oxygen-deficient rutile and $-\text{AlOOH}$. Such an orientation in stishovite would lead to more space between hydrogen and the neighboring oxygen atom, leading to weaker hydrogen bonding and higher wavenumber vibrations. Additionally, the tetrahedral hydrogarnet defect may not fully explain the sharp mode located at 1420 cm^{-1} . Only a portion of the population shifts to 1069 cm^{-1} as expected for the SiOH bend, but the remainder shifts only to 1383 cm^{-1} . Although our DFPT calculated SiOD modes match the 1069 cm^{-1} mode well, they provide no explanation for the 1383 cm^{-1} mode. Furthermore, the 2PT calculated phonon DoS for the tetrahedral

case at 25 °C (as shown in Figure 4) show that the tetrahedral case does not produce a mode near 1383 cm^{-1} when deuterated. This strongly suggests that alternate defects contribute the 1420 cm^{-1} / 1383 cm^{-1} modes. Situations involving either V_{Si} clusters, V_{O} , or other defects remain uninvestigated and could be the subject of future studies.

Our calculations target only a limited slice of the overall behavior observed in hydrous dense silica phases. Hydrous rutile-type SiO_2 , although stable in the pressure and temperature ranges we simulated here, transitions to CaCl_2 - and then niccolite-type SiO_2 structures at much lower pressures than its anhydrous counterpart, with increased capability to sequester hydrogen at each phase transition (Nisir et al., 2020). Whether additional tetrahedral arrangements become more stable in these higher-pressure phases, or square planar or other defect configurations become dominant remains to be seen. Calculations undertaken by Nisir et al. (2020) demonstrated that the volume increases observed in the CaCl_2 structure with increasing H_2O content are consistent with the experimental work of Spektor et al. (2016) and Nisir et al. (2017) when a tetrahedral configuration is selected. Additional work could reveal more nuanced behavior of Reutschi-like hydrogarnet defects in these more hydrous, higher-pressure phases, where an increased volume of V_{Si} could result in complex defect clusters.

5. Conclusions

Our QM calculations show that only one hydrogarnet-type defect state is important in stishovite at room temperature. This defect contains four OH groups arranged such that the hydrogen atoms have a tetrahedral geometry. The tetrahedral defect results in OH stretching modes that can fully account for the broad features observed via infrared spectroscopy, in contrast to earlier speculation of multiple, coexisting defect states. In addition to this, we find that a second defect state with square planar geometry becomes prominent at higher pressures and temperatures, coexisting with the tetrahedral defect in nearly equal proportion. These studies set the stage for future simulations of hydrogarnet-type defects in higher pressure polymorphs of dense silica that are stable in lower mantle and large planetary interior conditions.

Acknowledgments

The authors thank Charles Musgrave for helpful discussions.

W.A.G. was supported by the Liquid Sunlight Alliance, which is supported by the U.S. Department of Energy, Office of Science, Office of Basic Energy Sciences, Fuels from Sunlight Hub, under Grant DE-SC0021266. G.R.R. is thankful for National Science Foundation Grant EAR-2149559.

Open Research

All DFT calculations were carried out using the Vienna Ab Initio Simulation Package (VASP, version 5.4.4.18Apr17), a licensed software (details at: <https://www.vasp.at>). Two Phase Thermodynamics (2PT) calculations (Lin et al., 2003; Lin et al., 2010; Pascal et al., 2011) were used to produce the phonon DoS from

QM MD VASP calculations. Open Visualization Tool (OVITO), an open source visualization program, was used to convert QM MD output files into trajectories usable by 2PT (details at: <https://www.ovito.org>). Jmol: an open-source Java viewer for chemical structures in 3D (<http://www.jmol.org>) was used to visualize the vibrational modes produced from DFPT calculations. Visualization for Electronic and STructural Analysis (VESTA, version 3.5.5 26Sep2020), an open source visualization software, was used to produce the structural figures used in this work (details at: <https://jp-minerals.org/vesta/en>).

References

- Bjørheim, T. S., Kuwabara, A., & Norby, T. (2013). Defect Chemistry of Rutile TiO₂ from First Principles Calculations. *The Journal of Physical Chemistry C*, *117*(11), 5919–5930. <https://doi.org/10.1021/jp304146e>
- Blöchl, P. E. (1994). Projector augmented-wave method. *Physical Review B*, *50*(24), 17953–17979. <https://doi.org/10.1103/PhysRevB.50.17953>
- Blöchl, P. E., Jepsen, O., & Andersen, O. K. (1994). Improved tetrahedron method for Brillouin-zone integrations. *Physical Review B*, *49*(23), 16223–16233. <https://doi.org/10.1103/PhysRevB.49.16223>
- Bromiley, G. D., & Hilairet, N. (2005). Hydrogen and minor element incorporation in synthetic rutile. *Mineralogical Magazine*, *69*(3), 345–358. <https://doi.org/10.1180/0026461056930256>
- Grimme, S., Antony, J., Ehrlich, S., & Krieg, H. (2010). A consistent and accurate *ab initio* parametrization of density functional dispersion correction (DFT-D) for the 94 elements H-Pu. *The Journal of Chemical Physics*, *132*(15), 154104. <https://doi.org/10.1063/1.3382344>
- Grimme, S., Ehrlich, S., & Goerigk, L. (2011). Effect of the damping function in dispersion corrected density functional theory. *Journal of Computational Chemistry*, *32*(7), 1456–1465. <https://doi.org/10.1002/jcc.21759>
- Koudriachova, M. V., de Leeuw, S. W., & Harrison, N. M. (2004). First-principles study of H intercalation in rutile TiO₂. *Physical Review B*, *70*(16), 165421. <https://doi.org/10.1103/PhysRevB.70.165421>
- Kresse, G., & Furthmüller, J. (1996a). Efficiency of *ab-initio* total energy calculations for metals and semiconductors using a plane-wave basis set. *Computational Materials Science*, *6*(1), 15–50. [https://doi.org/10.1016/0927-0256\(96\)00008-0](https://doi.org/10.1016/0927-0256(96)00008-0)
- Kresse, G., & Furthmüller, J. (1996b). Efficient iterative schemes for *ab initio* total-energy calculations using a plane-wave basis set. *Physical Review B*, *54*(16), 11169–11186. <https://doi.org/10.1103/PhysRevB.54.11169>
- Kresse, G., & Hafner, J. (1993). *Ab initio* molecular dynamics for liquid metals. *Physical Review B*, *47*(1), 558–561. <https://doi.org/10.1103/PhysRevB.47.558>

- Kresse, G., & Hafner, J. (1994). *Ab initio* molecular-dynamics simulation of the liquid-metal–amorphous-semiconductor transition in germanium. *Physical Review B*, *49*(20), 14251–14269. <https://doi.org/10.1103/PhysRevB.49.14251>
- Kresse, G., & Joubert, D. (1999). From ultrasoft pseudopotentials to the projector augmented-wave method. *Physical Review B*, *59*(3), 1758–1775. <https://doi.org/10.1103/PhysRevB.59.1758>
- Libowitzky, E. (1999). Correlation of O-H Stretching Frequencies and O-H · · · O Hydrogen Bond Lengths in Minerals. *Chemical Monthly*, *130*, 1047–1059.
- Lin, S.-T., Blanco, M., & Goddard, W. A. (2003). The two-phase model for calculating thermodynamic properties of liquids from molecular dynamics: Validation for the phase diagram of Lennard-Jones fluids. *The Journal of Chemical Physics*, *119*(22), 11792–11805. <https://doi.org/10.1063/1.1624057>
- Lin, S.-T., Maiti, P. K., & Goddard, W. A. (2010). Two-Phase Thermodynamic Model for Efficient and Accurate Absolute Entropy of Water from Molecular Dynamics Simulations. *The Journal of Physical Chemistry B*, *114*(24), 8191–8198. <https://doi.org/10.1021/jp103120q>
- Lin, Y., Hu, Q., Meng, Y., Walter, M., & Mao, H.-K. (2020). Evidence for the stability of ultrahydrous stishovite in Earth’s lower mantle. *Proceedings of the National Academy of Sciences*, *117*(1), 184–189. <https://doi.org/10.1073/pnas.1914295117>
- Litasov, K. D., Kagi, H., Shatskiy, A., Ohtani, E., Lakshtanov, D. L., Bass, J. D., & Ito, E. (2007). High hydrogen solubility in Al-rich stishovite and water transport in the lower mantle. *Earth and Planetary Science Letters*, *262*(3–4), 620–634. <https://doi.org/10.1016/j.epsl.2007.08.015>
- Nisr, C., Chen, H., Leinenweber, K., Chizmeshya, A., Prakapenka, V. B., Prescher, C., Tkachev, S. N., Meng, Y., Liu, Z., & Shim, S.-H. (2020). Large H₂O solubility in dense silica and its implications for the interiors of water-rich planets. *Proceedings of the National Academy of Sciences*, *117*(18), 9747–9754. <https://doi.org/10.1073/pnas.1917448117>
- Nisr, C., Leinenweber, K., Prakapenka, V., Prescher, C., Tkachev, S., & Shim, S.-H. D. (2017). Phase transition and equation of state of dense hydrous silica up to 63 GPa. *Journal of Geophysical Research: Solid Earth*, *122*(9), 6972–6983. <https://doi.org/10.1002/2017JB014055>
- Nisr, C., Shim, S.-H., Leinenweber, K., & Chizmeshya, A. (2017). Raman spectroscopy of water-rich stishovite and dense high-pressure silica up to 55 GPa. *American Mineralogist*, *102*(11), 2180–2189. <https://doi.org/10.2138/am-2017-5944>
- Pascal, T. A., Lin, S.-T., & Goddard III, W. A. (2011). Thermodynamics of liquids: Standard molar entropies and heat capacities of common solvents

from 2PT molecular dynamics. *Phys. Chem. Chem. Phys.*, *13*(1), 169–181. <https://doi.org/10.1039/C0CP01549K>

Pawley, A. R., McMillan, P. F., & Holloway, J. R. (1993). Hydrogen in Stishovite, with Implications for Mantle Water Content. *Science*, *261*(5124), 1024–1026. <https://doi.org/10.1126/science.261.5124.1024>

Perdew, J. P., Burke, K., & Ernzerhof, M. (1996). Generalized Gradient Approximation Made Simple. *Physical Review Letters*, *77*(18), 3865–3868. <https://doi.org/10.1103/PhysRevLett.77.3865>

Perdew, J. P., Burke, K., & Ernzerhof, M. (1997). Generalized Gradient Approximation Made Simple [Phys. Rev. Lett. 77, 3865 (1996)]. *Physical Review Letters*, *78*(7), 1396–1396. <https://doi.org/10.1103/PhysRevLett.78.1396>

Ruetschi, P. (1984). Cation-Vacancy Model for MnO₂. *Journal of The Electrochemical Society*, *131*(12), 2737–2744. <https://doi.org/10.1149/1.2115399>

Shim, S.-H., Chizmeshya, A., & Leinenweber, K. (2022). Water in the crystal structure of CaSiO₃ perovskite. *American Mineralogist*, *107*(4), 631–641. <https://doi.org/10.2138/am-2022-8009>

Spektor, K., Nylén, J., Mathew, R., Edén, M., Stoyanov, E., Navrotsky, A., Leinenweber, K., & Häussermann, U. (2016). Formation of hydrous stishovite from coesite in high-pressure hydrothermal environments. *American Mineralogist*, *101*(11), 2514–2524. <https://doi.org/10.2138/am-2016-5609>

Spektor, K., Nylén, J., Stoyanov, E., Navrotsky, A., Hervig, R. L., Leinenweber, K., Holland, G. P., & Häussermann, U. (2011). Ultrahydrous stishovite from high-pressure hydrothermal treatment of SiO₂. *Proceedings of the National Academy of Sciences*, *108*(52), 20918–20922. <https://doi.org/10.1073/pnas.1117152108>